Thin Solid Films 558 (2014) 104–111

Contents lists available at ScienceDirect

Thin Solid Films

journal homepage: www.elsevier.com/locate/tsf

TaSiN nanocomposite thin films: Correlation between structure, chemical composition, and physical properties

G. Ramírez [a,b,*], D. Oezer [c], M. Rivera [d], S.E. Rodil [b], R. Sanjinés [c]

[a] Argonne National Laboratory, Energy Systems Division, Argonne, IL 60439, USA
[b] Instituto de Investigaciones en Materiales, Universidad Nacional Autónoma de México, Circuito Exterior s/n, CU, México D.F. 04510, Mexico
[c] Ecole Polytechnique Fédérale de Lausanne(EPFL), Institute of Condensed Matter Physics (ICMP), CH-1015 Lausanne, Switzerland
[d] Instituto de Física, Universidad Nacional Autónoma de México, México D.F. 04510, Mexico

ARTICLE INFO

Article history:
Received 1 July 2013
Received in revised form 21 February 2014
Accepted 26 February 2014
Available online 4 March 2014

Keywords:
Tantalum nitride
Silicon nitride
Thin films
Optical properties
Electrical properties
Nanocomposites

ABSTRACT

The structural and electronic properties of fcc-TaN/SiN_x nanocomposite thin films deposited by reactive magnetron sputtering have been investigated as function of the N and Si contents. Our studies have been mainly focused on three different types of nanocomposite $Ta_xSi_yN_z$ films based on: nitrogen deficient fcc-$TaN_{0.88}$, nearly stoichiometric fcc-TaN, and over-stoichiometric fcc-$TaN_{1.2}$ with the Si contents in the range from 0 to about 15 at.%. The optical properties were investigated by ellipsometric measurements, while the DC. electrical resistivity was measured using the van der Pauw configuration at 300 K. The optical measurements were interpreted using the standard Drude–Lorentz model. The results showed that the electronic properties are closely correlated with both the compositional and the structural modifications of the $Ta_xSi_yN_z$ films induced by the addition of Si atoms, and also depending on the stoichiometry of the starting fcc-TaN system. Thus, depending on both the nitrogen and the silicon contents, the fcc-$Ta_xSi_yN_z$ films can exhibit room temperature resistivity values ranging from 10^2 μΩ cm to about 6×10^4 μΩ cm.

Published by Elsevier B.V.

1. Introduction

The impressive number of outstanding physical, chemical and mechanical properties of transition metal nitrides MeN (Me stands for transition metal) makes then very attractive materials for many industrial applications as protective and decorative coatings [1,2]. As thin films MeN can be easily integrated in microelectronic devices as superconducting nanostructured thin films for single photon detectors [3,4], diffusion barriers in microelectronic devices [5–10], and also as materials for biomedical applications [11,12]. Among these systems, the Nb-N and Ta-N systems are interesting as they exhibit many different stable and metastable phases [13,14]. For example, TaN_x nitrides show different oxidation states, leading to phases such as: Ta_4N (orthorhombic), $Ta_6N_{2.57}$ (hexagonal), Ta_2N (hcp hexagonal), $TaN_{0.8}$ (hexagonal), ε-TaN (hexagonal WC type), δ-TaN (fcc NaCl-type), Ta_5N_6 (hexagonal), Ta_4N_5 (tetragonal), and Ta_3N_5 (orthorhombic)[14]. Each one of these phases presents different electronic properties, exhibiting a wide range of electrical resistivity values from about 10^2 to 10^4 μΩ cm [6,7,15].

The unusual combination of ionic, metallic and semiconductor-like bonding makes the conductivity of the TaNx materials very attractive for high temperature electrical contacts. However, their relatively weak thermal stability and resistance against oxidation limit the use of these nitrides to temperatures lower than 900 K. To further improve the performance and efficiency of microelectronic devices, nanocrystalline or quasi-amorphous ternary Me-Si-N systems have been considered. Thus, TiSiN, TaSiN, and WSiN films have been largely investigated as diffusion barrier in Cu interconnections. Depending on the deposition techniques (Physical Vapor Deposition or Chemical Vapor Deposition), the process parameters, and the chemical composition, $Ta_xSi_yN_z$ films exhibit good chemical and thermal stability up to 1300 K as well as electrical resistivity values ranging from 3×10^2 μΩ cm to 8×10^4 μΩ cm [5,16–25]. Nevertheless, less information is available about the optical properties; the optical functions of the $Ta_xSi_yN_z$ thin films have not been reported in the literature. Earlier studies on the TaSiN films reported in the literature have focused on their functional properties and very little on their fundamental properties.

Most of the fcc-NaCl type MeN crystals are interstitial compounds. While keeping their fcc crystal structure, they can accommodate high concentrations of nitrogen vacancies in the non-metal sublattice; only few nitrides such as ZrN_x, HfN_x and TaN_x have been reported as cation deficient and/or compounds with antisite substitutions [3,26–28].

In the previous paper [29], we presented the study of the optical and electrical properties of $Ta_xSi_yN_z$ thin films, finding that the evolution of the Ta-Si-N system from a solid solution to a nanocomposite material

* Corresponding author at: Argonne National Laboratory, Energy Systems Division, Argonne, IL 60439, USA. Previously at: Instituto de Investigaciones en Materiales, Universidad Nacional Autónoma de México.
E-mail addresses: jramirez@anl.gov, enggiova@hotmail.com (G. Ramírez).

http://dx.doi.org/10.1016/j.tsf.2014.02.079
0040-6090/Published by Elsevier B.V.

due to the silicon inclusion could be followed by the changes in the opto-electronic properties. In that study, the electronic and optical properties were modeled by the Grain Boundary Scattering Model and the Drude–Lorentz model, respectively and the analysis of the electron density and optical estimated conductivity clearly showed the transition from a solid solution to a nanocomposite for the stoichiometry and over-stoichiometric films.

In the present paper, more details about the growth conditions are included and it is also shown that the direct measured optical or electronic properties, i. e. refractive index and resistivity presented different trend as a function of the Si content that gives insight into the structure of the $Ta_xSi_yN_z$ films.

Due to the phase diversity of the Ta-N system, the choice of a single phase is essential in order to better understand the physical properties of two phases TaN_x/a-SiN nanocomposites as their physical and functional properties are intimately related. For these studies, the fcc NaCl-type TaN phase was selected and special attention was paid to the chemical composition of the fcc TaN_x phase. Thus, three different series of $Ta_xSi_yN_z$ films were prepared based on sub-stoichiometric TaN_x (with $x \leq 1$), nearly stoichiometric TaN_x ($x \approx 1$), and over-stoichiometric TaN_x ($x \geq 1$) compounds. From the fundamental point of view, it is well known that the physical properties are influenced by the structural disorder (vacancies, substitutional, antisites, and interstitial atoms), phase composition, and film morphology. The knowledge of the relations between the microstructure and the physical properties of disordered single- or two-phase nanocomposite films leads to a better understanding and improving of their functional properties.

2. Experimental

Three different series of $Ta_xSi_yN_z$ films were deposited using two different reactor chambers. Each magnetron sputtering system is equipped with two confocal planar magnetron sources positioned with their axes at a 25° or 30° angles off the vertical, the substrate-target distances were fixed at 100 mm. The substrates are mounted on a rotary sample holder manipulator to insure film homogeneity. The deposition chamber is connected to a turbo molecular pump through an adaptive pressure controller valve, which allows fixing the final total pressure in the sputtering chamber. Mass flow regulators are fitted for controlling independently the sputtering Ar and the reactive N_2 gases. All the TaSiN films have been deposited using individual Si (99.999 at.%) and Ta (99.95 at.%) targets. The targets diameters were 5 cm.

For the first series namely series A, a high DC power of 400 W was applied to the Ta target while a variable RF power ranging from 60 to 340 W was applied to the Si target in order to change the Si content (C_{Si}) in the $Ta_xSi_yN_z$ films. Before the deposition of the films the residual pressure in the sputtering chamber was typically lower than 10^{-4} Pa. The substrate temperature was kept constant at 653 K, the total working pressure, $P_T = (P_{Ar} + P_{N2})$, was fixed at 0.4 Pa. The N_2/Ar flow ratio was initially varied, until the conditions to obtain the fcc-NaCl phase were obtained (N_2/Ar = 6/14). Under these conditions, $Ta_xSi_yN_z$ samples with $0.42 < z < 0.44$ (referred in the paper as $Ta_xSi_yN_{0.44}$ nitrogen deficient films) were obtained.

For the second and third film series (namely series B and C) the power applied to the Ta target was about 100 W, while the DC power on the Si target was varied between 0 and 60 W. The residual pressure in the reactor chamber was typically less than 10^{-4} Pa. The films were deposited in a mixed (Ar + N_2) atmosphere. During the deposition, the total pressure P_T and the substrate temperature T_s were kept constant at 0.5 Pa and 753 K, respectively. The series B and C have been deposited using N_2/Ar flow ratios of 2/13 and N_2/Ar = 7/13, respectively, leading to $Ta_xSi_yN_z$ films with $0.49 \leq z \leq 0.51$ (referred as nearly stoichiometric $Ta_xSi_yN_{0.5}$ films or series B) and over-stoichiometric films with $0.54 \leq z \leq 0.57$ (denoted as $Ta_xSi_yN_{0.56}$ films or series C).

The film thickness measured by profilometry (Tencor PH50) was typically 0.8–1.2 μm for the series B and C and about 1.2 μm for the series A (Dektak 150). The chemical composition of the $Ta_xSi_yN_z$ films was obtained by electron probe microanalyses (EPMA) and X-ray Photoelectron Spectroscopy, XPS measurements. The XPS measurements were performed using a commercial VG Microtech Multilab ESCA 2000. The contaminant element was found to be oxygen (≤5 at.%). The crystallographic phase was determined by X-ray diffraction using monochromatized Cu Kα radiation. The crystallite or grain sizes of the films were estimated from Bragg Brentano (BB-XRD) configuration measurements. The surface morphology of the films was investigated by using two different STM systems, a Jeol JSPM-4210 working in air (for series A) and an UHV VT-SPM Omicron (for series B and C).

The optical properties of the films of series A were investigated by ellipsometric measurements in the photon energy range of 1.5–5.0 eV using an Uvisel Jobin-Yvon DH10 ellipsometer and the data analysis was performed using the DeltaPsi2 software. The series B and C were characterized using an Alpha-SE-Woollam ellipsometer (1.3–3.3 eV). All the investigated $Ta_xSi_yN_z$ films were optically opaque, thus ellipsometric measurements provide directly the complex dielectric function $\varepsilon(E) = \varepsilon_1(E) + i\varepsilon_2(E)$ of the films as well as the refractive index $n(E)$ and the extinction coefficient $k(E)$. The small effects due to the surface roughness and surface oxidation were not considered in the evaluation of the dielectric function.

For the resistivity measurements, the films were deposited onto highly resistive (>800 Ω cm) Si or on oxidized Si wafers and the measurements were performed using the van der Pauw method in the temperature range between 20 K and 300 K.

3. Results

3.1. Film deposition

Due to the complexity of the Ta-N phase diagram [13,14] for each deposition system a preliminary study of the Ta-N system was performed to optimize parameters leading to the deposition of single fcc δ-TaN phase.

3.1.1. Series A

Fig. 1 shows the XRD patterns of TaN_x films for various N_2/Ar flow ratios. As the N_2/Ar flow ratio increased from 0 to 0.64, the TaN_x films exhibited different single or mixed phases. At low N_2 flows, the films presented primarily the β-phase. However at $N_2/Ar = 0.43$, the TaN_x films crystallized in the hexagonal ε-TaN phase while the δ-TaN phase (NaCl-type) was obtained at a slightly higher N_2/Ar flow ratio around 0.5. For the deposition of series A films, the N_2/Ar flow ratio was fixed at 0.43 and the RF power of the Si target was varied from 0 to 340 W. Using this flow ratio, the results indicated that the addition of even

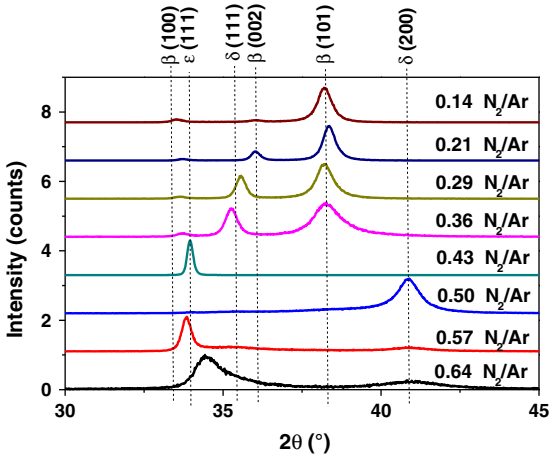

Fig. 1. Diffractograms for the TaN_x films of series A as a function of the N_2/Ar flow ratio.

small quantities of Si (few at.%) promoted the crystallization of the fcc δ-TaN phase in contrast to the pure ε-TaN obtained without the Si addition. Fig. 2 shows the Si, Ta and N atomic concentrations of the $Ta_xSi_yN_z$ films as a function of the power applied to the Si target. The Si (Ta) content increased (decreased) progressively as the Si target power was increased, reaching a maximum Si content of 11.7 at.%. The oxygen content in the films was about 5 at.% without any correlation with the Si content. Regarding the N content, it decreased from 44.6 to 42.0 at.%. Thus, under the aforementioned deposition conditions, the $Ta_xSi_yN_z$ are nitrogen deficient films with $0.42 < z < 0.446$. These films are referred in the paper as $Ta_xSi_yN_{0.44}$ samples or sub-stoichiometric films.

3.1.2. Series B and C

In order to produce stoichiometric and over-stoichiometric films, a careful analysis of the discharge parameters as a function of the N_2/Ar flow ratio was done. The TaN_x films were deposited in constant current mode fixed at 300 mA, at a substrate temperature of 753 K and total pressure (Ar + N_2) of 0.5 Pa. The reactive sputtering process of the TaN_x films was characterized by the variation of the target voltage V_{Ta} as a function of the N_2/Ar flow ratio, as well as the drop of the chamber pressure ΔP upon ignition of the discharge. Fig. 3a shows the variation of V_{Ta} and ΔP as a function of N_2/Ar. The V_{Ta} increased abruptly first, and then progressively decreased when N_2/Ar was increased from 0 to 1.6. The ΔP *vs* N_2/Ar curve exhibits a peak at about $N_2/Ar = 0.125$ and a plateau between $N_2/Ar = 0.2$ and 1.2. Similar trends were observed in earlier studies of TaN_x films deposited by reactive sputtering [28]. The variations of V_{Ta} and ΔP were respectively explained in terms of surface target nitridation and nitrogen consumption by the fresh Ta layers deposited at the substrate and the walls of the sputtering chamber [30,31]. In the present study, the maximum of the N_2 consumption was observed near the formation of stoichiometric TaN layers; N_2/Ar about 0.15. Meanwhile, for N_2/Ar ratios between 0.2 and 1.2, the N_2 consumption remained more or less constant. The increase of V_{Ta} was mainly due to a decrease in the target secondary-electron emission coefficient γ due to the progressive nitridation of the Ta target. In cold cathode discharges, $V_{Ta} = E_0 / (g\gamma)$ where E_0 is the energy required to create one ion-electron pair (typically $E_0 \approx 30$ eV for Ar magnetron discharge) and $0 < g < 1$ is a geometric factor determined by the system [28,30,31]. Fig. 3b shows an estimation of γ as a function of N_2/Ar considering $E_0 = 30$ eV and $g = 0.5$. It is observed that γ decreased from about 0.215 to 0.17 exhibiting three different linear regimes: a) γ decreased quickly from 0.215 to 0.19 for N_2/Ar between 0 and 0.2, b) between $N_2/Ar = 0.2$ and 0.6, γ decreased moderately, and c) above $N_2/Ar = 0.6$, γ decreased gradually. In addition, the N/Ta atomic ratio curve indicates that TaN_x films with $x \approx 1$ are achieved at about $N_2/Ar = 0.154$, then x increased progressively up to 1.45 when the flow ratio is increased up to 1.6.

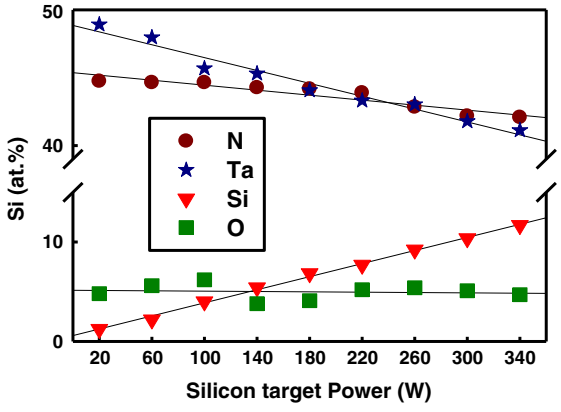

Fig. 2. Total atomic percentages of Ta, N, Si and O of $Ta_xSi_yN_z$ films of series A estimated by XPS.

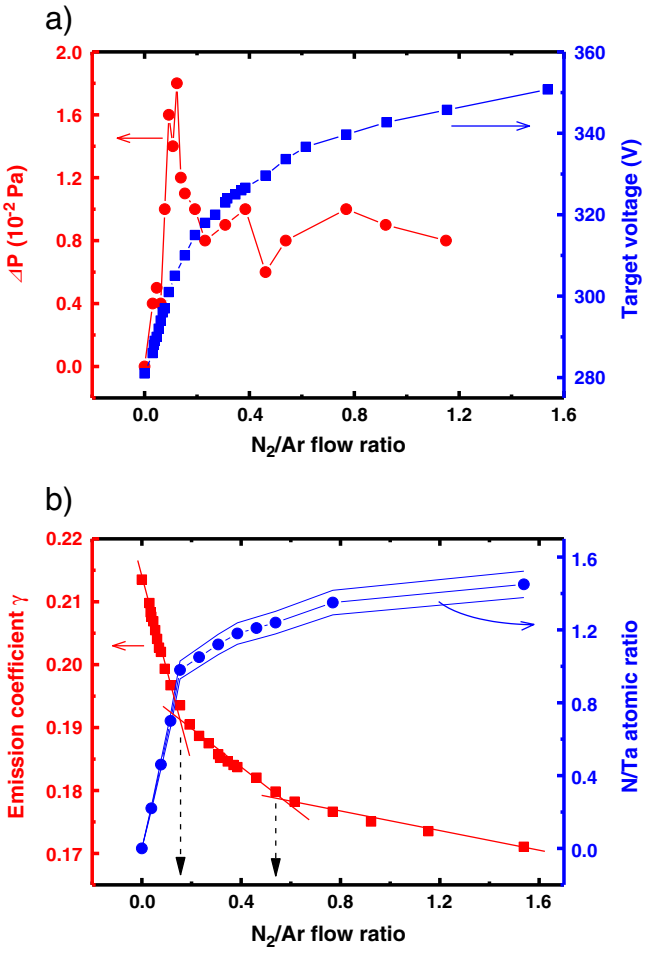

Fig. 3. a) Variation of the Ta target voltage V_{Ta} and of the pressure drop ΔP_{tot} upon igniting the discharge as a function of the N_2/Ar flow ratio during the reactive magnetron sputtering of TaN_x films of series B and C. b) Emission coefficient *g* and N/Ta atomic composition ratio vs. the N_2/Ar flow ratio. The selected N_2/Ar flow ratio values for the deposition of near- and over-stoichiometric TaN_x films are indicated.

XRD data revealed (no shown) that in the N_2/Ar flow ratio range between 0 and 0.15, a series of lower nitrides are formed (Ta_4N, Ta_2N and δ-TaN), the hexagonal Ta_2N is formed at a flow ratio of $N_2/Ar = 0.077$. In the flow ratio range of 0.154–0.54, the films were crystallized in the single phase fcc $\delta - TaN_x$ with $1.0 \le x \le 1.25$. Finally, for $N_2/Ar \ge 0.6$ the TaN_x films were composed of a mixture of $\delta - TaN$ and hexagonal TaN phases. It is worth noting that the N_2/Ar flow ratio ranges associated with the formation of these nitrides are strongly correlated with the nitridation state of the Ta Target as suggested by the variations of γ. Consequently, for the deposition of $Ta_xSi_yN_z$ films of series B and C, the N_2/Ar flow ratio was fixed at 0.154 and 0.54, respectively, and the DC power of the Si target was changed from 0 to 60 W. Fig. 4 illustrates the chemical composition of the obtained $Ta_xSi_yN_z$ films. In both series B and C, the Si (Ta) content increased (decreased) progressively as the DC power applied to the Si target was increased from 0 to 60 W. The nitrogen content changed within a limited range of $0.49 \le z \le 0.51$ for series B and of $0.54 \le z \le 0.57$ for series C. Thus, in the present paper these films are denoted as nearly stoichiometric $Ta_xSi_yN_{0.5}$ films (series B) and over-stoichiometric $Ta_xSi_yN_{0.56}$ films (series C).

3.2. Morphology of TaSiN films

Under the deposition conditions aforementioned, pure TaN_x films and $Ta_xSi_yN_z$ films containing low Si atomic concentration were crystallized in the fcc-NaCl type of structure and exhibit a marked columnar-

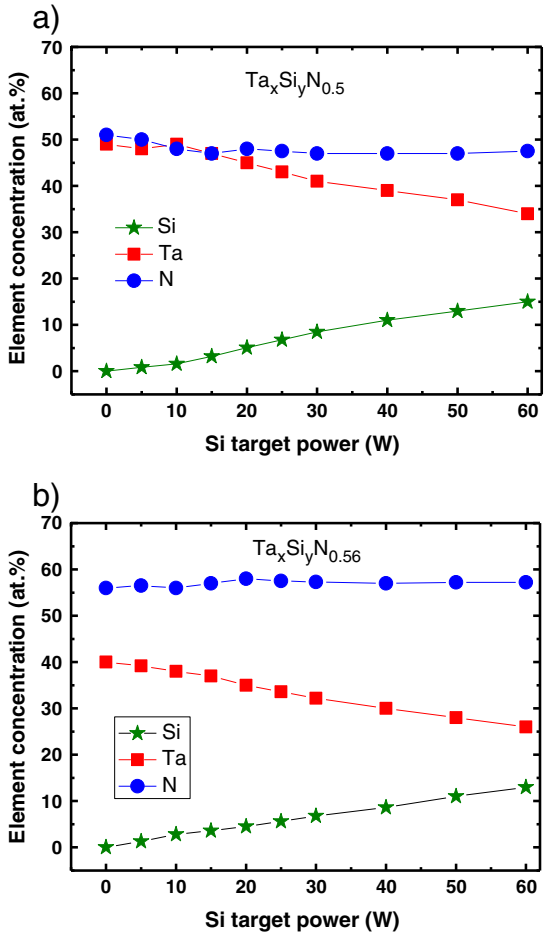

Fig. 4. Total atomic percentages of Ta, N and Si of $Ta_xSi_yN_z$ of a) series B and b) series C estimated by EPMA measurements.

like morphology with crystallites elongated in the growth direction. The progressive addition of the Si atoms lead to important structural modifications. For instance, Fig. 5 illustrates the surface morphology of the nearly-stoichiometric $TaN_{1.02}$ and $Ta_xSi_yN_{0.5}$ samples investigated by STM measurements. At the early stages of the deposition of the $TaN_{1.02}$ film, small crystallites nucleated near the substrate interface. The surface of a 50 nm thick film was characterized by the presence of dense clusters composed of small grains (size of 10–20 nm); the irregular shape of the grains suggests the presence of randomly oriented crystallites (Fig. 5a). As the thickness of the $TaN_{1.02}$ film increased, the film developed a columnar structure, as shown in Fig. 5b for a 1200 nm thick film, which is characterized by the presence of large compact domains (size of 200 nm); each domain is composed of grains of 10–20 nm in size. The presence of both square shaped domains and squared shaped grains suggests the occurrence of (100) orientated TaN crystallites perpendicular to the substrate plane. In contrast to that, the surface morphology of the 1100 nm thick $Ta_xSi_yN_{0.5}$ film with the Si content $y = 0.11$ presents a fine-grained dense structure with small grains 10 nm in size as illustrated in Fig. 5c.

XRD patterns measured at grazing incident of $Ta_xSi_yN_{0.5}$ films (series B) are illustrated in Fig. 6a. The observed peaks are attributed to the cubic δ-TaN phase. GI-XRD measurements revealed the presence of small crystallites randomly oriented. In addition, the XRD patterns recorded in the Bragg–Brentano configuration (BB-XRD) revealed that the films exhibit (100) preferential texture (see Fig. 6b). As the Si content in the films increased, the average crystallite size decreased and the marked (100) orientation was strongly reduced. Similar trends have also been observed in $Ta_xSi_yN_{0.56}$ films or series C (no shown). Fig. 7 shows the average crystallite size calculated from the BB-XRD measurements for series B and C. The average crystallite size was estimated by the Scherrer's formula using the integral bread. The method does not take into account the contribution of the strain in the width estimation of the XRD peak; nevertheless it gives a good estimation of the crystallite size in particular for small crystallites.

In the case of series A films, the (100) preferential texture was not obstructed even at the highest Si content of 11 at.% investigated in the present work, as illustrated in Fig. 8a. These films exhibited crystallites with average sizes of the order of 4–12 nm without correlation with the Si content as displayed in Fig. 8b. Nevertheless, the addition of Si improves the density of the films, as observed by STM images. Fig. 9 shows the STM images of the under-stoichiometric films as a function of the Si content. The surface of the $Ta_xSi_yN_{0.44}$ films with low Si content (Fig. 9a) exhibited large compact domains at about 0.5–1.0 μm in size with a root mean square roughness of rms = 36 nm typical of columnar structure containing voids. As the Si content increased (from 2.2 to 11.7 at.%), the rms roughness decreased to 5.2 nm and the surface was characterized by a more dense morphology.

3.3. Optical properties

As mentioned above, the $Ta_xSi_yN_z$ films were optically opaque; therefore it was possible to obtain the energy dependence of the complex refractive index directly from the ellipsometric measurements. In the previous paper, the dispersion relations were shown for the three series. However, here we show that by choosing a single wavelength, it is possible to observe different trends as a function of the Si content for each series.

The values of the refractive index n_{630} and extinction coefficient k_{630} at a fixed wavelength of 630 nm as a function of the Si content are reported in Fig. 10 for the three series; 630 nm was chosen arbitrarily

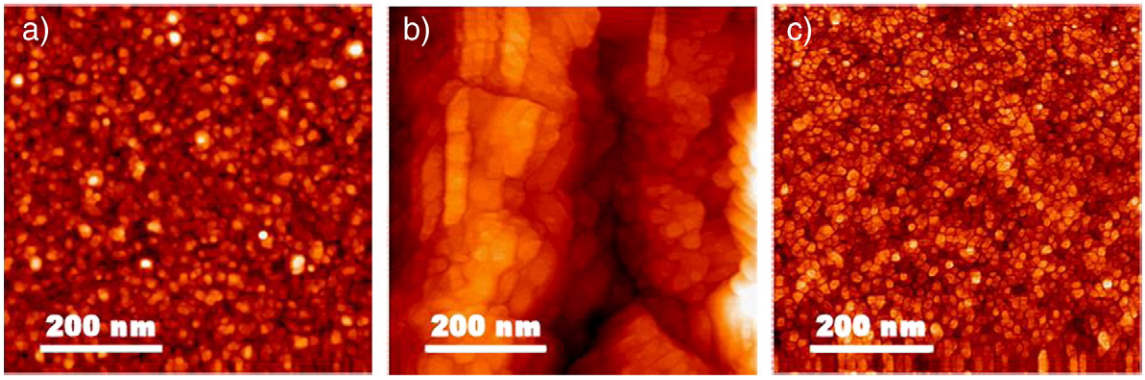

Fig. 5. Scanning tunneling microscopy (STM) images (600 × 600 nm^2) of: a) 50 nm thick $TaN_{1.02}$ film, b) 1200 nm thick $TaN_{1.02}$ film, and c) 1100 nm thick $Ta_xSi_yN_{0.5}$ with Si content y = 0.11.

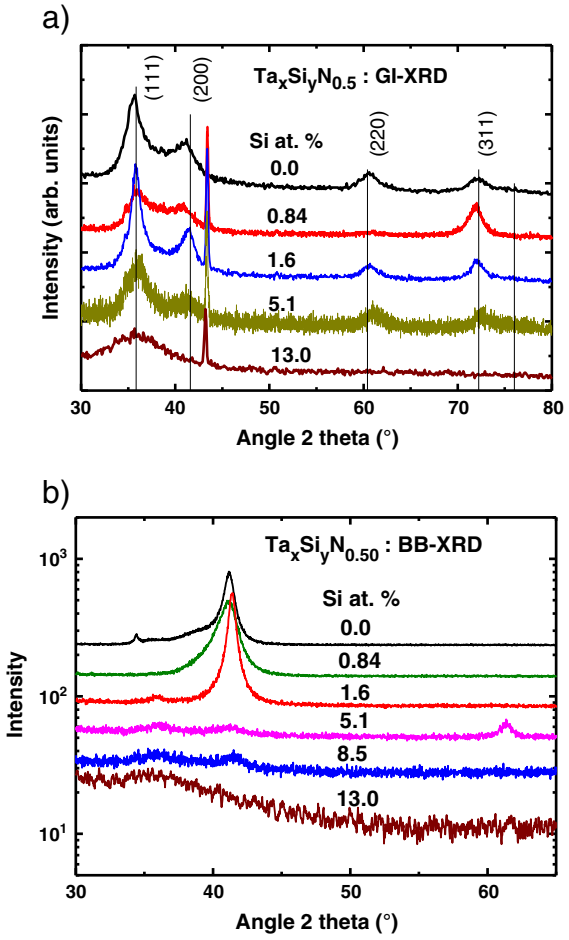

Fig. 6. XRD patterns obtained from $Ta_xSi_yN_{0.5}$ films. a) In grazing incidence configuration (GI-XRD at 4°) and b) Bragg-Brentano scans (BB-XRD).

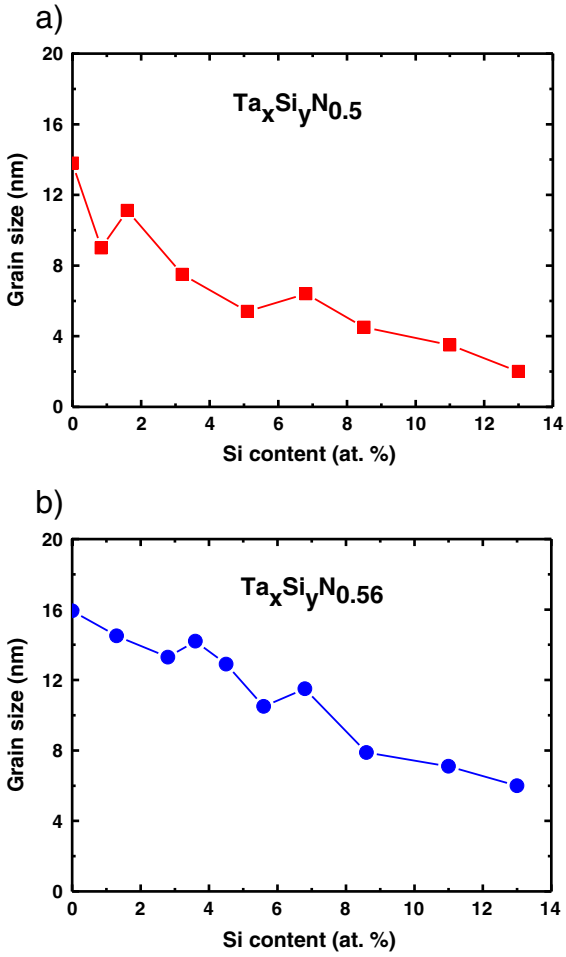

Fig. 7. Average grain size of a) $Ta_xSi_yN_{0.5}$ films and b) $Ta_xSi_yN_{0.56}$ films obtained from BB-XRD measurements.

since it is close to the standard fixed wavelength ellipsometers. In Fig 10a, it can be seen that for the sub-stoichiometric series A films, the refractive index varied in an oscillatory-like way between 2.7 and about 3.7. Meantime, the extinction coefficient changed very little ($k_{630} = 3 \pm 0.3$). The irregular changes of n_{630} as function of the Si content seem to be correlated to the changes in the grain size observed in these films. By comparing Figs. 9 and 10a, the changes of n_{630} as a function of the Si content suggest that $Ta_xSi_yN_{0.44}$ films with large crystallite sizes (8–12 nm) exhibit more metallic behavior (low n values) than those with small crystallite sizes (4–6 nm), which exhibit less metallic behavior (large n values). In the case of series B, (Fig. 10b), the extinction coefficient k_{630} decreased progressively from about 3 to 1.7, meanwhile the refractive index changed little (3.0 ± 0.4) when the Si content increased. Finally, for Series C (10c); k_{630} also decreased from 2.5 to 0.6 but the refractive index increased from 1.8 to 2.9.

3.4. Electrical properties

The room temperature (RT) DC resistivity (ρ_{RT}) as a function of the Si content for all the investigated films is plotted in semi-log scale in Fig. 11. The electrical resistivity of the series A changed very little as a function of the Si content, ρ_{RT} varied in the range of 130 to 260 μΩ cm without correlation with the Si content. In the case of the films of series B, ρ_{RT} increased progressively from 230 up to 965 μΩ cm as the Si content in the films increased from 0 to 15 at.%. The highest resistivity values were observed for series C. In this case, two regimes were clearly observed; below 5 at.%, ρ_{RT} exhibited values in the range of $(0.9–1.5) \times 10^3$ μΩ cm. Meanwhile, for silicon contents between 6 at.% and 13 at.%, the resistivity increased abruptly up to about 5×10^4 μΩ cm.

4. Discussion

The observed trends in the refractive index, extinction coefficient and electrical and optical resistivity of $Ta_xSi_yN_z$ films are closely related to the compositional and microstructural modifications of the $Ta_xSi_yN_z$ films due to the stoichiometric composition of the fcc δ-TaN and the addition of Si atoms. In general, sputter-deposited Me-N systems are polycrystalline and exhibit elongated grains in the growth direction. The addition of even small quantities of Si, can lead to significant modifications in the chemical bonding and the film morphology. Whether a single-phase or composite multi-phased system is formed, depends on the chemical reactivity of the involved atoms and on the deposition parameters. The incorporation of Si atoms into the MeN lattice represents the introduction of additional structural defects, which perturb the subsequent grain formation. Further increase of the Si content can lead to the progressive reduction of the lateral and vertical sizes of the growing crystallites due to the segregation of Si atoms towards the grain boundaries resulting in nanocomposite thin films [32–38].

The Ta-N system has been investigated in details by Shin et al. [3,28]. In good agreement with Shin's results, our study confirms that sputter deposited TaN_x thin films can crystallize in the fcc δ-TaN phase over a wide chemical composition range of $0.9 < x < 1.3$. The fcc TaN_x has been reported as a cation deficient and/or a compound with antisite substitutions [3,28]. In polycrystalline materials, the scattering sites are mainly grain boundary regions and lattice defects (N and Ta

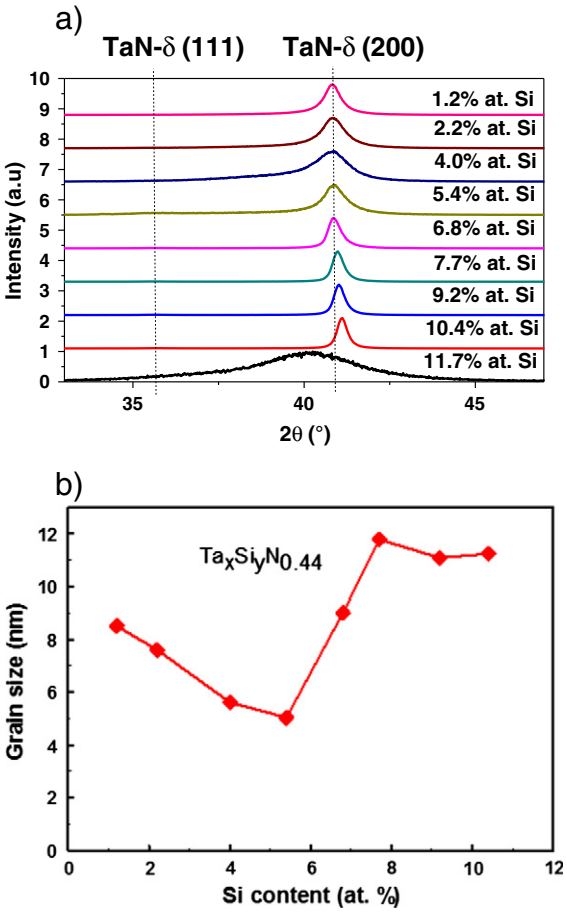

Fig. 8. XRD patterns of a) $Ta_xSi_yN_{0.44}$ films as a function of the Si content and b) grain size.

vacancies, N and Ta antisites, and interstitial atoms in the case of fcc δ-TaN). According to the disorder scattering model proposed by Nordheim [39], the electron scattering rate is proportional to both the density of states at the Fermi level $N(E_F)$ and to the concentration of defects. The variation of $N(E_F)$ with the concentration of defects (or chemical composition) depends on details of the band structure. Yu el at [40] have investigated the electronic structure of N-rich fcc-TaN_x compounds and the formation energies of point defects. The calculations indicate that Ta vacancies have the lowest formation energy and that such defects induce larger modifications in the band structure of the N-rich TaN_x compared to that of stoichiometric TaN. With increasing the density of Ta vacancies, the DOS at the Fermi level monotonically decreases, thus Ta vacancies can act as acceptors-sites and electron localization at the Ta-vacancies is responsible for the metal to non-metal transition observed in fcc δ-TaN_x nitrides. By comparing the optical and electrical properties of near stoichiometric $TaN_{1.02}$ and N-rich TaN_x films, the presence of high density of Ta vacancies and N atoms in antisite positions may explain the higher resistivity values observed in these films. Our results are consistent with the theoretical predictions reported by Yu et al. [40].

Concerning the Ta-Si-N system, our results indicate that the formation and nature of TaN/SiN_x nanocomposite film depends on the N content in films. In $Ta_xSi_yN_{0.5}$ and $Ta_xSi_yN_{0.56}$ films, the n and k, as well as ρ_{RT}, are strongly influenced by the changes in the chemical composition exhibiting a continuous loss of their metallic character (k decreased and ρ_{RT} increased). The strong increase in ρ_{RT} values from about 230 μΩ cm up to 965 μΩ cm in $Ta_xSi_yN_{0.5}$ and from about 10^3 μΩ cm to 5×10^4 μΩ cm in $Ta_xSi_yN_{0.56}$ films with increasing the Si content suggests the formation of nanocomposite films constituted by small metallic-like TaN grains embedded in a dielectric SiN_x matrix [34,36]. Theoretical modeling of the dielectric function of these films by using the Drude–Lorentz model revealed that the diminution in crystallite size was accompanied by an important diminution in the density of free carriers; the lattice defects and grain boundary regions determine the main free path of electrons [29]. The decrease in the conductivity is tentatively attributed to the changes in the density of point defects (Ta and N vacancies, Ta and N antisites) due to the strong affinity of N atoms to combine with Si atoms to form SiN_x near the surface of the crystallites and at the grain boundary regions. A progressive decrease of the density of N antisites, increases the density of Ta vacancies, which acts as acceptors increasing the localization of the electrons. Further insight on the transport properties of these films was obtained from temperature dependence resistivity measurements [29], where the application of the grain boundary scattering model indicated that at the Si contents higher than about 4.6 at.%, the electron scattering at the grain boundaries becomes important. Thus, if the N_2/Ar flow ratio is adequate for the deposition of near stoichiometric fcc δ-TaN or N-rich δ-TaN_x thin films, the addition of Si atoms leads to the formation of nc-TaN/a-SiN_x nanocomposite-like films composed of nanocrystallites (nc) of TaN surrounded by an amorphous SiN_x layer. The SiN_x layer behaves like an electrically insulating layer.

In contrast to that, in the case of N-deficient fcc δ-TaN_x films, the addition of Si atoms lead to the formation of solid solution TaN_x-SiN_x films with different film structure and physical properties. The crystallite size and the columnar growth with (100) texture were not efficiently hindered by the addition of Si. The low chemical composition dependence of n, k and electrical resistivity observed in $Ta_xSi_yN_{0.44}$ films clearly indicate that the Si segregation in N-deficient TaN_x films does not lead to the formation of an efficient electrically insulating SiN_x thin layer. Due to the lower N content in the films, besides the SiN_x insulating phase, there is a possibility of the formation of conducting Ta_ySi_x [22] thin layers at the grain boundary regions too. Therefore, the weak dependency of the resistivity on the Si content for these coatings can be attributed to the frequent percolation of the conducting TaN_x crystallites and $TaSiN_x$ crystallites surrounded by conducting Ta_ySi_x thin layers. Similar results have been reported by Jedrzeovski

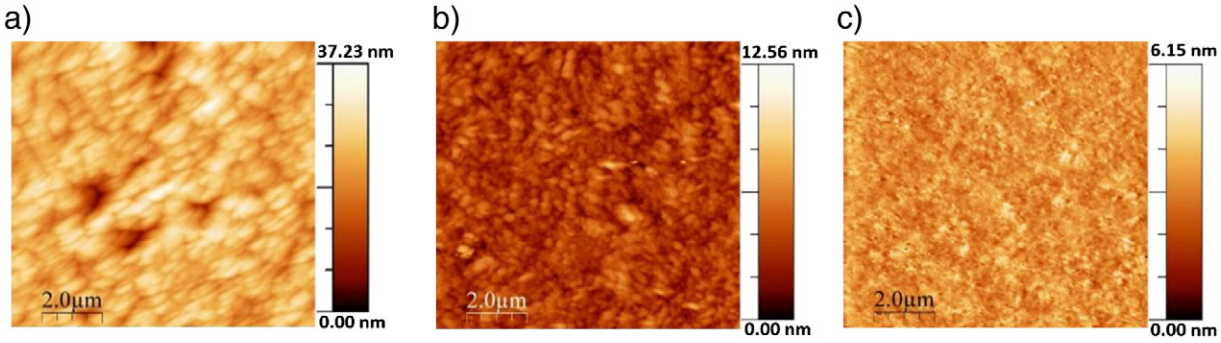

Fig. 9. STM images en $Ta_xSi_yN_{0.44}$ as a function of the silicon content. a) 2.2% at., b) 6.9% at., c) 11.7% at.

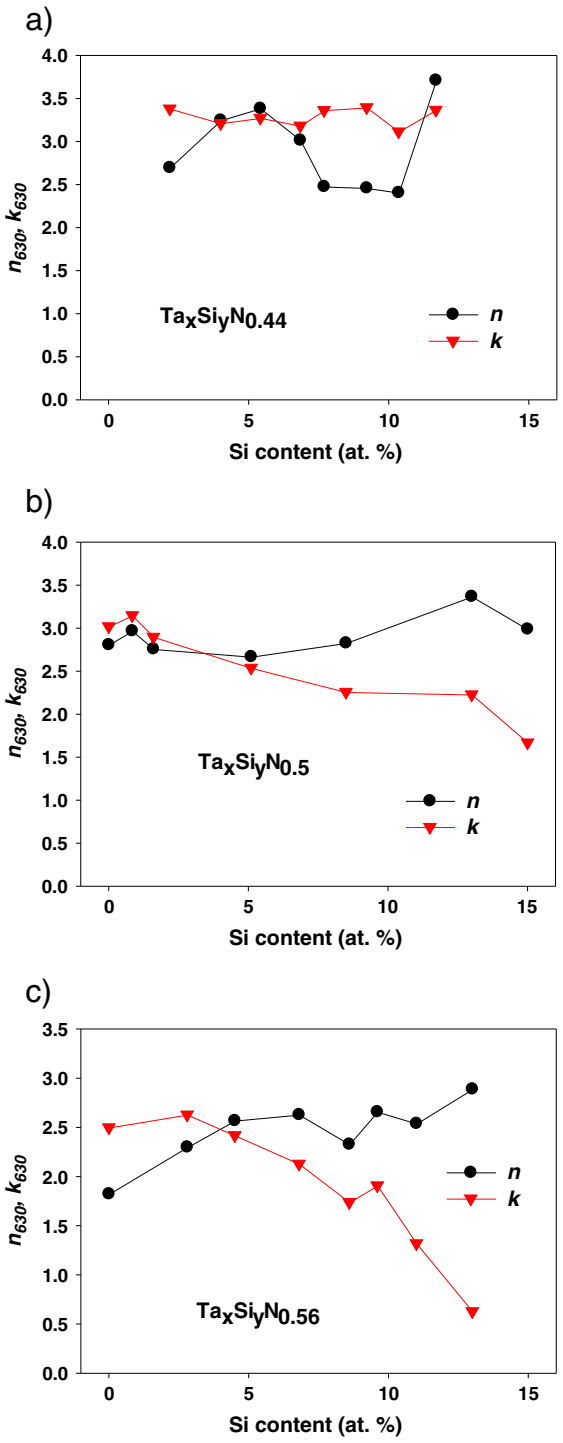

Fig. 10. Values of refractive index n and extinction coefficient k at a wavelength of 630 nm vs Si content in a) $Ta_xSi_yN_{0.44}$, b) $Ta_xSi_yN_{0.5}$ and c) $Ta_xSi_yN_{0.56}$ films.

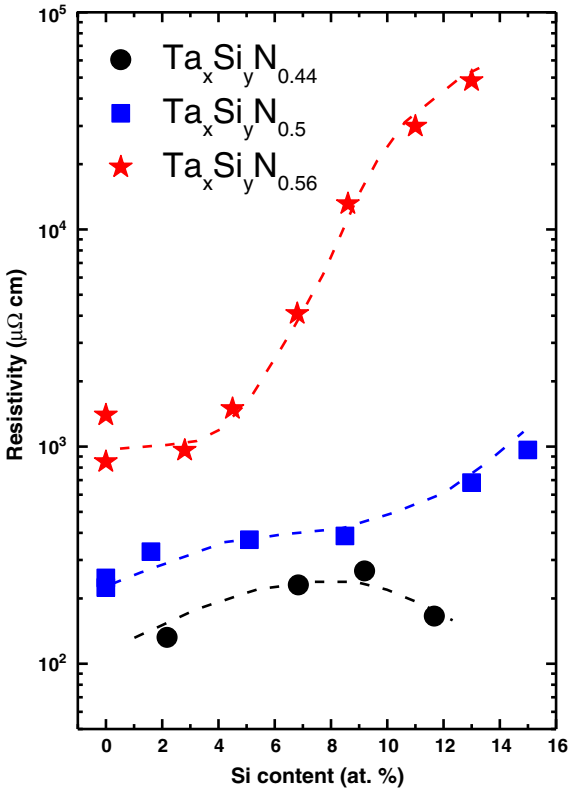

Fig. 11. RT DC. electrical resistivity obtained from van de Pauw configuration measurements *vs* Si content of $Ta_xSi_yN_{0.44}$, $Ta_xSi_yN_{0.5}$ and $Ta_xSi_yN_{0.56}$ films.

et al. [37] for nanocomposite TiN/SiN_x films and, more recently for ZrN/SiN_x thin films deposited using bias voltages of −150 V and at substrate temperatures of 510 K and 720 K [38].

5. Summary and conclusions

The structural, electrical and optical properties of $Ta_xSi_yN_z$ thin films deposited by reactive magnetron sputtering were investigated as a function of both the nitrogen and silicon contents. The deposition parameters were optimized to obtain fcc-TaN (NaCl-type) as the main nitride phase. Pure fcc-TaN_x thin films can accommodate large concentration of N and Ta vacancies and antisite substitutions ($0.9 < x < 1.3$). Based on these results, three different series of $Ta_xSi_yN_z$ films were prepared, namely a) sub-stoichiometric $Ta_xSi_yN_{0.44}$ films, b) near stoichiometric $Ta_xSi_yN_{0.5}$ films and c) nitrogen-rich $Ta_xSi_yN_{0.55}$ with the Si contents in the range of 0 to 15 at.%.

In the case of sub-stoichiometric $Ta_xSi_yN_{0.44}$ films, the (100) preferential texture was not obstructed even at the highest Si content of 11 at.%. Nevertheless, the addition of Si improves the density of the films. These films exhibited metallic behavior with room temperature electrical resistivity values in the range of 130 to 260 μΩ cm without correlation with the Si content. The refractive index n_{630} changes from 2.3 up to 3.4, the extinction coefficient changes very little ($k_{630} = 3 \pm 0.3$). Therefore, Si segregation in N-deficient TaN_x films does not lead to the formation of a homogeneous electrically insulating SiN_x thin layer between the metallic TaN crystallites.

In the case of near-stoichiometric $Ta_xSi_yN_{0.5}$ and nitrogen-rich $Ta_xSi_yN_{0.56}$ films, the average crystallite size decreases and the marked (100) orientation was strongly reduced as the Si content in the films increased. The strong increase in ρ_{RT} values from about 230 μΩ cm up to 970 μΩ cm in $Ta_xSi_yN_{0.5}$ and from about 10^3 μΩ cm to 5×10^4 μΩ cm in $Ta_xSi_yN_{0.56}$ films with increasing the Si content suggested the formation of nanocomposite films constituted by small metallic TaN grains embedded in a dielectric SiN_x matrix. In agreement with the observed decrease in the extinction coefficient k_{630} from about 3 to 1.7 in $Ta_xSi_yN_{0.5}$ and from 2.5 to 0.6 in $Ta_xSi_yN_{0.56}$, when the Si content was increased.

In conclusion, these studies shed light on the structural and electrical properties of $Ta_xSi_yN_z$ nanocomposite thin films based on fcc-TaN (NaCl-type of structure). Highly conductive or insulating $Ta_xSi_yN_z$ films are considered as promising materials for applications as electrically diffusion barriers. The electrical properties of $Ta_xSi_yN_z$ thin films can be fine-tuned by judicious adjustment of the N and Si contents.

Acknowledgments

The authors are grateful to the Swiss National Science Foundation and PAPIIT-UNAM 103910 for the financial support; G. Ramirez acknowledges the support of CONACYT for scholarship during his PhD studies. S.E. Rodil thanks the technical support from H. Zarco for the electronic maintenance, A. Tejeda for the XRD support and L. Huerta for the XPS analysis.

References

[1] L.E. Toth, Transition Metal Carbides and Nitrides, Academic, New York, 1971.
[2] H. Holleck, J. Vac. Sci. Technol. A 4 (1986) 2661.
[3] C.-S. Shin, D. Gall, Y.-W. Kim, P. Desjardins, I. Petrov, J.E. Greene, J. Appl. Phys. 90 (2001) 2879.
[4] J.P. Sprengers, A. Gaggero, D. Hasin, S. Jahanmirinejad, G. Frucci, F. Mattiolli, R. Leoni, J. Beetz, M. Lermer, M. Kamp, S. Höfling, R. Sanjinés, A. Fiore, Appl. Phys. Lett. 99 (2011) 181110.
[5] A.E. Kaloyeros, E. Eisenbraun, Annu. Rev. Mater. Sci. 30 (2000) 363.
[6] T. Riekkinen, J. Molarius, T. Laurila, A. Nurmela, I. Suni, J.K. Kivilauhti, Microelectron. Eng. 64 (2002) 289.
[7] S.M. Rossnagel, J. Vac. Sci. Technol. B 20 (2002) 2328.
[8] M. Wittmer, Appl. Phys. Lett. 36 (1980) 456.
[9] J.M. Daughton, Thin Solid Films 216 (1992) 162.
[10] X. Sun, E. Kolawa, J. Chen, J.S. Reid, M.A. Nicolet, Thin Solid Films 236 (1993) 347.
[11] Y.X. Leng, H. Sun, P. Yang, J.Y. Chen, J. Wang, G.J. Wan, N. Huang, X.B. Tian, L.P. Wang, P.K. Chu, Thin Solid Films 398–399 (2001) 471.
[12] S.M. Aouadi, M. Debessai, J. Vac. Sci. Technol. B 22 (2004) 1134.
[13] G.I. Oya, Y. Onodera, J. Appl. Phys. 47 (1976) 2833.
[14] T.B. Massalski, Binary Alloy Phase Diagrams, vol. 3, The Materials Information Society, Materials Park, OH, 1990. 2703.
[15] S.M. Kang, S.G. Yoon, S.J. Suh, D.H. Yoon, Thin Solid Films 516 (2008) 3568.
[16] J.S. Reid, E. Kolawa, R.P. Ruiz, M.A. Nicolet, Thin Solid Films 236 (1993) 319.
[17] D.J. Kim, Y.T. Kim, J.W. Park, J. Appl. Phys. 82 (1997) 4847.
[18] Y.J. Lee, B.S. Suh, M.S. Kwom, C.O. Park, J. Appl. Phys. 85 (1999) 1927.
[19] Y.S. Suh, G.P. Heuss, V. Misra, Appl. Phys. Lett. 80 (2002) 1403.
[20] F. Letendu, M.C. Hugon, B. Agius, I. Vickridge, C. Berthier, J.M. Lameille, Thin Solid Films 513 (2006) 118.
[21] J.O. Olowolafe, I. Rau, K.Mr. Unruh, C.P. Swann, Z.S. Jawad, T. Alford, Thin Solid Films 365 (2000) 19.
[22] R. Hübner, M. Hecker, N. Mattern, V. Hoffmann, K. Wetzig, H. Heuer, Ch. Wenzel, H.J. Engelmann, D. Gehre, E. Zschech, Thin Solid Films 500 (2006) 259.
[23] C. Cabral Jr., K.L. Saenger, D.E. Kotecki, J.M.E. Harper, J. Mater. Res. 15 (2000) 194.
[24] P. Alén, T. Aaltonen, M. Ritala, M. Leskelä, T. Sajavaara, J. Keinonen, J.C. Hooker, J.W. Maes, J. Electrochem. Soc. 151 (2004) G523.
[25] K.-M. Jung, M.-S. Jung, Y.-B. Kim, D.-K. Choi, Thin Solid Films 517 (2009) 3837.
[26] M. Yoshitake, T. Yotsuya, S. Ogawa, Jpn. J. Appl. Phys. 31 (1992) 4002.
[27] B.O. Johansson, U. Helmersson, M.K. Hibbs, J.E. Sundgren, J. Appl. Phys. 58 (1985) 3104.
[28] C.S. Shin, Y.-W. Kim, D. Gall, J.E. Greene, I. Petrov, Thin Solid Films 402 (2002) 172.
[29] D. Oezer, G. Ramirez, S.E. Rodil, R. Sanjines, J. Appl. Phys. 112 (2012) 114302.
[30] I. Petrov, A. Myers, J.E. Greene, J.R. Abelson, J. Vac. Technol. A 125 (1994) 2846.
[31] Z. Wang, S.A. Cohen, J. Vac. Sci. Technol. A 17 (1999) 77.
[32] C.S. Sandu, R. Sanjinés, M. Benkahoul, F. Medjani, F. Lévy, Surf. Coat. Technol. 201 (2006) 4083.
[33] E. Martinez, R. Sanjinés, O. Banakh, F. Lévy, Thin Solid Films 447–448 (2004) 332.
[34] R. Sanjinés, M. Benkahoul, C.S. Sandu, P.E. Schmid, F. Lévy, J. Appl. Phys. 98 (2005) 123511.
[35] C.S. Sandu, F. Medjani, R. Sanjinés, Rev. Adv. Mater. Sci. 15 (2007) 173.
[36] C.S. Sandu, S. Harada, R. Sanjinés, A. Cavaleiro, Surf. Coat. Technol. 204 (2010) 1907.
[37] P. Jedrzejowski, B. Baloukas, J.E. Klemberg-Sapieha, L. Martinu, J. Vac. Sci. Technol. A 22 (2004) 725.
[38] C.S. Sandu, N. Cusnir, D. Oezer, R. Sanjinés, J. Patscheider, Surf. Coat. Technol. 204 (2009) 969.
[39] L. Nordheim, Ann. Phys. 9 (1931) 607.
[40] L. Yu, C. Stampfl, D. Marshall, T. Eshrich, V. Narayanan, J.M. Rowell, N. Newman, A.J. Freeman, Phys. Rev. B 65 (2002) 245110